Peptization of boehmites with different peptization index: An electron microscopy and synchrotron small-angle X-ray scattering study

Lucie Speyer, Séverine Humbert, Thomas Bizien, Vincent Lecocq, Antoine Hugon

▶ **To cite this version:**

Lucie Speyer, Séverine Humbert, Thomas Bizien, Vincent Lecocq, Antoine Hugon. Peptization of boehmites with different peptization index: An electron microscopy and synchrotron small-angle X-ray scattering study. Colloids and Surfaces A: Physicochemical and Engineering Aspects, 2020, 603, pp.125175. 10.1016/j.colsurfa.2020.125175 . hal-03118683

HAL Id: hal-03118683
https://ifp.hal.science/hal-03118683

Submitted on 18 Jul 2022

HAL is a multi-disciplinary open access archive for the deposit and dissemination of scientific research documents, whether they are published or not. The documents may come from teaching and research institutions in France or abroad, or from public or private research centers.

L'archive ouverte pluridisciplinaire **HAL**, est destinée au dépôt et à la diffusion de documents scientifiques de niveau recherche, publiés ou non, émanant des établissements d'enseignement et de recherche français ou étrangers, des laboratoires publics ou privés.

Distributed under a Creative Commons Attribution - NonCommercial 4.0 International License

Version of Record: https://www.sciencedirect.com/science/article/pii/S0927775720307688
Manuscript_aef6cd27574b2f4abc72907ecfa569b3

Peptization of boehmites with different peptization index: an electron microscopy and synchrotron small-angle X-ray scattering study

Lucie Speyer[a*1], Séverine Humbert[a], Thomas Bizien[b], Vincent Lecocq[a], Antoine Hugon[a]

[a] IFPEN Lyon, Rond-point de l'échangeur de Solaize, 69390 Solaize, France

[b] Synchrotron SOLEIL, beamline SWING, L'Orme des Merisiers, 91190 Saint-Aubin, France

L. Speyer: lucie.speyer@univ-lorraine.fr

S. Humbert: severine.humbert@ifpen.fr

T. Bizien: thomas.bizien@synchrotron-soleil.fr

V. Lecocq: vincent.lecocq@ifpen.fr

A. Hugon: antoine.hugon@ifpen.fr

[1] Corresponding author : Lucie Speyer +33 (0)3 72 74 25 40. Present address: Institut Jean Lamour, UMR 7198 CNRS – Université de Lorraine, 2 allée André Guinier, BP 50840, 54011 Nancy, France.

© 2020 published by Elsevier. This manuscript is made available under the CC BY NC user license
https://creativecommons.org/licenses/by-nc/4.0/

Abstract

Boehmite AlOOH is used as a precursor for the preparation of mesoporous gamma-alumina, which is of well-known interest for use as a catalyst support in petroleum refinery. The fabrication of the shaped supports is usually decomposed in several steps: synthesis of boehmite, preparation of a paste by kneading, extrusion of the paste and finally calcination to obtain the alumina phase. Mesoporous alumina is a complex hierarchical porous network, whose growth is influenced by each step of the process, and needs to be clearly understood to optimize the catalytic performances. This paper is focused on the peptization of boehmite, an important step in the fabrication which corresponds to the beginning of the kneading. Peptization is carried out in liquid phase, from two boehmites batches with different abilities to be peptized (peptization index) and with different acid/aluminum ratios. The as-obtained suspensions are characterized by coupling electron microscopy and small-angle X-ray scattering, which bring an accurate description of the samples at their different levels of structural organization. A multi-scale mechanism of peptization is then proposed. Finally, we will discuss the study of the measure of boehmites peptization index, and confirms the textural features which are relevant for the behavior of a boehmite in an acid medium.

Keywords: alumina, boehmite, peptization, small-angle X-ray scattering

1. Introduction

Boehmite AlOOH is used as a precursor for the synthesis of γ-alumina, which is of primordial interest, amongst others, as a support for petroleum refining catalysts [1]. These supports have to be shaped in order to meet for example the pressure requirements of the industrial equipments. The fabrication of the shaped supports is usually decomposed in several steps: synthesis of boehmite, preparation of a paste by acid then basic kneading, extrusion of the paste and calcination to obtain the alumina phase. Mesoporous alumina and boehmite are quite complex porous networks, often described as agglomerates of aggregated crystallites [2-7]. Each step of the fabrication process can influence the formation of this final porous texture, and a precise understanding of the underlying phenomena is of great importance. Indeed the support porous texture directly affects the deposition of the active phase of the catalyst and its mass transfer properties, so its catalytic performances.

We focus, in this paper, on the peptization of boehmite, *i. e*. its dispersion in acid medium. It consists, for the extrudable paste preparation , in a first step called kneading. Plus, liquid phase peptization is employed to determine the ability of boehmite to be dispersed in acid medium, called peptization index (PI), which is an important aspect to take into account for the preparation of the supports.

Boehmite crystallites have their surfaces covered with hydroxyl groups [8] which, in the case of peptization, become positively charged and create a double-layer repulsion. The expected effects of this repulsion are then a modification in the interactions governing the boehmite structure. The repulsive interactions are shown to lead to the separation of the aggregates [9-16] and even, for high acid/aluminum ratios, to a separation of the crystallites [11,16]. A partial dissolution of boehmite has been observed by several groups through the detection of aluminum cations in suspension [9] or adsorbed on the boehmite surface [17,18]. However, the peptization has no influence on the crystallite size [10-12,16]. These effects are expected to modify the textural properties of boehmite: the size of the particles decreases with peptization [11], so as the pore size and the width of the pore size distribution [10].

All these modifications essentially depend on two factors. The first one is the acid/aluminum ratio used for peptization, which enhances its effects if higher [13,16], the second one is the PI of boehmite. Karouia *et al*. reported a fundamental difference between a low peptizable boehmite, whose structure is almost modified after peptization, and a highly peptizable boehmite which loses its structural integrity after peptization in the same conditions [12].

In this work, we study the influence of these two major parameters on the peptization of boehmite. Suspensions are prepared from boehmites with different PI, and different acid/aluminum ratios. They are studied by two techniques: scanning transmission electron microscopy (STEM), which brings a direct observation of the influence of peptization on the morphology of boehmite, and, for the first time at the best of our knowledge, by synchrotron small-ange X-ray scattering (SAXS). This latter method is widely used to study hierarchical systems of various nanoparticles, especially their synthesis, aggregation or gelation [19-22]. It can provide information about the size and fractal dimension of the different levels of organization of the materials, *i. e.* the crystallites, aggregates and agglomerates. STEM and SAXS coupling is expected to bring a multi-scale description of the effects of peptization on the boehmite organization. Lastly, SAXS is used to study the method of measure of PI, in order to bring further information about this method and in order to confirm which characteristics of a boehmite lead to a better ability to be dispersed in an acid medium.

2. Materials and methods

2.1. Raw boehmites

The two raw boehmites are industrial products provided by IFPEN. As suspensions of boehmites at the end of synthesis, they are denoted as B1 and B2 regarding their peptization index.

2.2. Peptization index

Several methods have been proposed for the evaluation of the PI of boehmites. They are usually based on the peptization of a sample and its separation, by centrifugation, in two parts called peptizable (supernatant) and non peptizable (sediment). The relative mass of boehmite contained in these two parts defines the value of PI [12]. In this work, PI is measured with a method developed by IFPEN and based on refractometry. A suspension of boehmite in a solution of nitric acid is prepared in order to reach an equivalent HNO_3/Al_2O_3 of 10%wt and an equivalent concentration of alumina of 10%wt. The suspension is first homogenized by magnetic stirring, then stirred with an Ultra-Turax disperser during 5 minutes (13000 rpm) and centrifuged during 10 minutes (6000 rpm). The refraction index of the supernatant is measured, and provides a determination of the quantity of boehmite in the peptizable part and then the calculation of the PI value. By this method, PI for B1 and B2 are respectively 77% and 100%.

2.3. Preparation of the peptized samples

The preparation of peptized samples is based on the conditions of measurement of the peptization index. For each boehmite, three suspensions were prepared with a concentration of alumina of 10%wt, and by varying the HNO_3/Al_2O_3 ratio with values of 5%wt (samples B1-p5 and B2-p5), 10wt% (samples B1-p10 and B2-p10) and 20wt% (samples B1-p20 and B2-p20). The suspensions were stirred as described in part 2.2., but not centrifuged.
In order to bring further information on the PI measurement, the sample B1-p10 was centrifuged. As previously mentioned, the supernatant is the peptizable part (sample B1-p10-p) and the sediment the non peptizable part (sample B1-p10-np).

2.4. Characterization

Boehmites (dried at 80°C during 24h) are analyzed by X-ray diffraction measurements carried out with a PANalytical Xpert Pro diffractometer ($\lambda(Cu_{K\alpha 1})$ = 1.5406 Å by Scherrer's equation applied on the [020] and [120] peaks. The obtained values are respectively 2.7 nm and 3.9 nm for B1, and 2.7 and 3.2 nm for B2.

STEM micrographs are collected with a FEI NOVA Nano SEM microscope operating at 15 keV and TEM micrographs with a JEOL 2100F TEM microscope operating at 200 keV. STEM analysis enables a better contrast and is well adapted for the low-magnification observations, and TEM analysis brings a better resolution, especially for the observation of well-dispersed samples. Suspensions of raw boehmites at the end of co-precipitation, and peptized samples, are diluted in water in order to obtain a concentration around 10^{-4} %vol for SEM observations and 5.10^{-5} %vol for TEM observations. A drop of the dilution is deposited on a copper grid with a holey carbon film, the excess of liquid was absorbed with a paper towel and the grid was dried with an infrared lamp before introduction in the microscope.

SAXS analysis is carried out on the SWING Beamline at synchrotron SOLEIL. The incident beam energy was 10 keV as often used for aqueous samples. It allowed optimizing the scattered intensity relatively to the sample thickness. All suspensions (raw boehmites at the end of synthesis, and peptized samples) are preserved in a cooler between their preparation and the analysis. They are pumped out from a beaker using a peristaltic pump, and thus pushed through a 1.5 mm diameter quartz capillary which is perpendicularly crossed by the beam. Some samples turned to a gel state, and are then analyzed with an automatic solid sample changer between two mica windows with a thickness of 500 µm.

In order to cover a wider range of q values, three sample-detector distances (0.55 m, 3 m and 6 m) are employed. The scattering images are recorded using a AVIEX PCCD170170 detector. To increase the statistic of the scattering intensity, ten images are acquired at each detector-sample configuration. The acquisition time is function of the configuration and was chosen in order not to saturate the detector.

Through 1D reduction, raw data were corrected with respect to: acquisition time, geometrical effects like the projection of the detector plane on the sphere with radius equal to the sample-detector distance, the incoming-photon flux and finally averaged to increase the statistic. Data were also corrected by either the mica windows scattering and the sample thickness for the gel

samples, or the scattering from capillary filled with water and the capillary diameter for the liquid samples.

Finally, in order to calibrate the intensity in absolute units, *i.e.* expressed as differential scattering cross section per unit volume in cm^{-1}, water was measured and a correction factor has been calculated from the ratio between the theoretical data and the experimental data.

SAXS results obtained on raw boehmites B1 and B2 are plotted on Fig. 1.

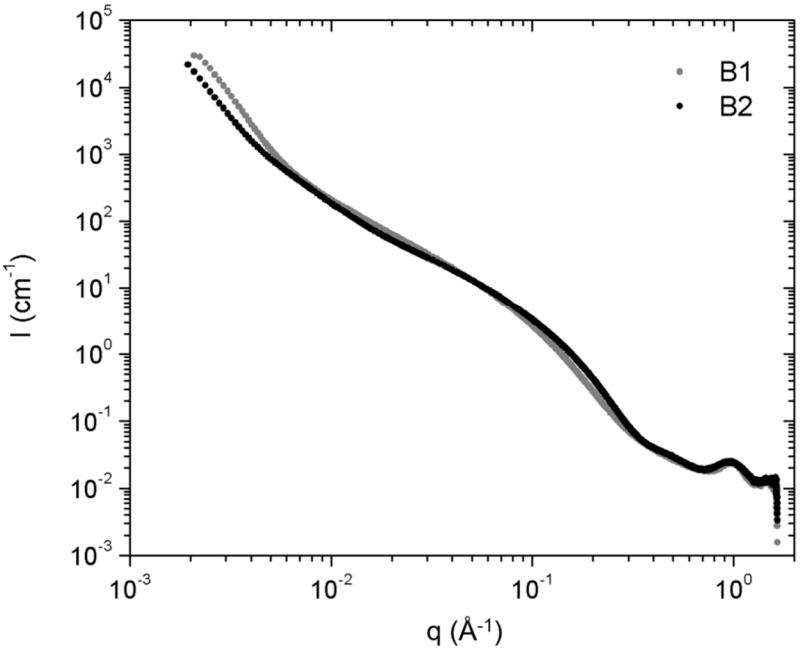

Fig. 1

Given the shape of the curves (two inflections of the scattered signal and typical slopes) and based on boehmite knowledge, the boehmite suspensions can be considered as fractal system with primary particles, aggregates and agglomerates scales [23].

Indeed, three different domains can be observed on these curves. At low q (between 10^{-1} $Å^{-1}$ and $3x10^{-1}$ $Å^{-1}$), a Porod regime can be observed with a slope of -4, characteristic of smooth surface. At medium q (between $1x10^{-2}$ $Å^{-1}$ and $8x10^{-2}$ $Å^{-1}$), another power-law regime with a slope closed to -2 is characteristic of fractal clusters. At small q (inferior to $8x10^{-2}$ $Å^{-1}$), another Porod-type regime is observed with a slope closed to -3.5, representative of rough surface. The cross-over of the first two domains can lead to the determination of the particle correlation length, respectively 1.0 nm and 1.1 nm for B1 and B2 samples. Unfortunately, the presence of agglomerates make it difficult to measure the aggregate size, usually obtained

from the cross-over of the power-law fractal domain and the Guinier plateau. However, we did the measurement anyway, which give aggregate correlation lengths of 14.3 nm and 12.8 nm respectively for B1 and B2 samples.

In order to extract data for the different structure levels more easily and more robustly, another approach has been implemented. SAXS curves were fitted using the Beaucage model [24-26] which supposes a multi-level organization of the particles. The diffused intensity follows Eq. (1):

$$I(q) \cong \sum_{i=1}^{n} G_i . \exp\left(\frac{-q^2 . R_{g,i}^2}{3}\right) + B_i . \exp\left(\frac{-q^2 . R_{g,i+1}^2}{3}\right) . \left(\frac{(\mathrm{erf}(q . k_i . R_{gi}/\sqrt{6}))^3}{q}\right)^{P_i} \quad (1)$$

where q is the diffusion vector, $G_i = N_d . r_e^2 . \rho_e^2 . V^2$ (N_d is the number density of particles, r_e the electron radius, ρ_e the electron density difference between the particle and its environment and V the average particle volume), B_i is a prefactor and k_i an empirical factor both depending on the exponent P_i, $R_{g,i}$ is the gyration radius of the particle and erf() the error function. i corresponds to a level of structural organization, and n is the total number of levels of organization: in this work, we assume a three-level organization (primary particles, aggregates and agglomerates) in accordance with the presumed morphology of boehmite. For agglomerates and aggregates, the model provides the fractal dimension, associated to the exponent P_i (the slope in usual logarithmic representation), and the gyration radius of the agglomerate, aggregate or primary particle.

A nonlinear Least-Squares Algorithm DN2FB [27] was used for the curve fitting. It allowed to obtain both the adjusted parameters and their standard deviation estimated from the variance-covariance matrix. Variation coefficient can also be calculated by the ratio between the standard deviation and the parameter value. The exponent P_3 relative to the particle scale was fixed to -4 in order to eliminate one parameter in the fitting procedure, after checking this assumption by hand measurements.

The degree of aggregation, z_{ag}, reflects the number of primary particles in an average aggregate and can be obtained from the ratio of the Guinier prefactors for the aggregate and primary levels G_2/G_3 [25,26]:

$$z_{ag} = \frac{G_2}{G_3} \quad (2)$$

On the same principle, the degree of agglomeration, z_{agglo}, reflects the number of aggregates in an average agglomerate and can be obtained from the ratio of the Guinier prefactors for the agglomerate and aggregate levels G_1/G_2 [25, 26]:

$$z_{agglo} = \frac{G_1}{G_2} \quad (3)$$

Variation coefficient for G_1 and G_2 values are quite small (2-10%), so that z_{agglo} becomes quite sensitive. Besides, variation coefficient of G_3 is more significant (6-34%), compared to the one of Rg_2 and Rg_3 (1-5%). Then, we preferred to follow the degree of aggregation thanks to the following equation to obtain a better precision:

$$z_{ag} = \left(\frac{R_{g,2}}{R_{g,3}}\right)^{P_2} \quad (4)$$

This formula is not appropriate for the agglomerates as they can be very dense and show a surface fractal ($P_1 > 3$).

The curve fitting for sample B1 is shown as an example on Fig. 2.

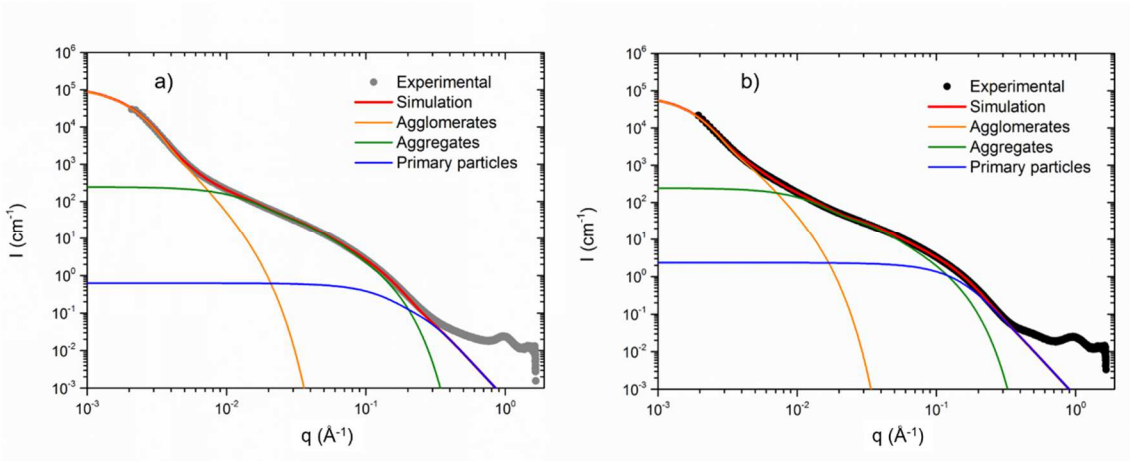

Fig. 2

3. Results and discussion

3.1. Characterization of raw boehmites

Fig. 3 shows STEM micrographs (SEM microscope) at different magnifications for the raw boehmites B1 and B2.

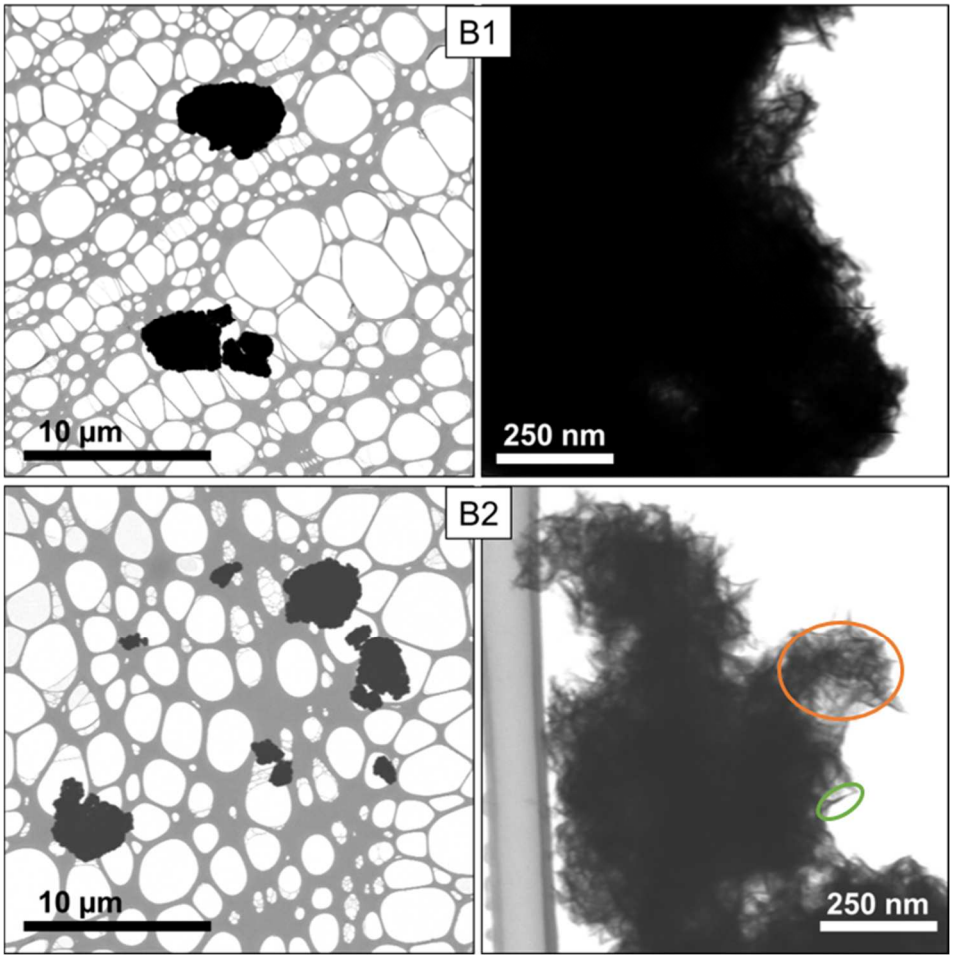

Fig. 3

The low-magnification micrographs show, for both samples, dense and large particles measuring several micrometers. They seem to be constituted of smaller dense assemblies (several hundred nanometers): one of them is marked with an orange ellipse. B2 is constituted with large and smaller particles, as B1 show more uniform large particles. It could contribute to explain why B2 has a higher peptization index: these smaller particles should be easier to disperse in acid medium. At higher magnifications, a quasi-fibrillar morphology is observed for the two boehmites. X-ray diffraction gives crystallite sizes of 2.7 nm for B1 and B2 along (020) direction, and of 3.9 nm for B1 and 3.2 nm for B2 along (120) direction. The length of the observed branched fibrils (one of them is marked with a green ellipse) is several tens of nanometers: they are then polycrystalline and constituted with aggregated crystallites. This is an usual description for nanocrystalline boehmites. For B2, the spatial arrangement of these fibrils is more aerated than for B1.

Concerning the SAXS results (see Fig. 1), the two curves identically show three linear domains. At high q values ($q > 10^{-1}$ Å^{-1}), the Porod domain with a q^{-4} variation is associated with the primary particles. The intermediate q domain (5.10^{-3} Å^{-1} < q < 10^{-1} Å^{-1}) describes the aggregates, and the low q domain is attributed to the agglomerates. Such multi-level structures have been studied for example by Schaefer *et al.* [23]. Data providing from curve fitting with the Beaucage model (gyration radius R_g, exponent P) and the agglomeration and aggregation degrees are indicated in Table 1.

Table 1. Gyration radius R_g, exponent P of agglomerates, aggregates and primary particles and degrees of agglomeration and aggregation for the samples B1 and B2. Errors (±2σ) are indicated in brackets.

Sample	Agglomerates			Aggregates			Primary particles	
	R_g (nm)	P	z_{agglo}	R_g (nm)	P	z_{ag}	R_g (nm)	P
B1	100 *(3)*	3.70 *(0.07)*	498	12.3 *(0.3)*	1.94 *(0.01)*	88	1.22 *(0.08)*	4.0
B2	107*(3)*	3.39 *(0.03)*	325	13.6 *(0.3)*	1.90 *(0.02)*	87	1.29 *(0.03)*	4.0

For each boehmite, the gyration radius of the primary particles is around 1.2-1.3 nm. These values are consistent with crystallite sizes measured by X-ray diffraction, and with values obtained from the cross-overs (1.0 and 1.1 nm). Indeed, for platelet objects, the gyration radius can be calculated thanks to the following formula [28]:

$$R_g = \left(\frac{a^2+b^2+c^2}{12}\right)^{0.5} \quad (5)$$

with a, b and c the lateral dimensions of the platelet. Estimating crystallites dimensions (around 3 nm for each dimension) from XRD leads to gyration radii around 1.5 nm.

Primary particles are then attributed to the boehmite crystallites. These crystallites are assembled to form the branched fibrils observed by microscopy. SAXS gives average gyration radii, for the following level of organization *i. e.* the aggregates, around 12-13 nm, which is consistent with the dimensions of the branched fibrils. As mentioned with the case of crystallites, gyration radii can not be directly related with the real dimensions of the considered particle, but only with the order of magnitude. Indeed, in order to better compare to STEM results, equivalent end-to-end distance of these aggregates can be calculated by the following formula [29]:

$$\xi = R_g \left[\left(1 + \frac{2}{df}\right) \left(2 + \frac{2}{df}\right) \right]^{0.5} \quad (6)$$

For B1 and B2 samples, it leads to dimensions of 31 nm and 34 nm respectively, which agree with STEM images.

The values of the exponents for the aggregates indicate that they are mass fractals [30], in good accordance with values reported in the literature on the aggregation of nanoparticles to form branched systems [19-21,30-32]. The resolution of the SEM microscope is not sufficient to visualize the branched arrangement of the crystallites within the aggregates, which then appears as linear fibrils. For mass fractals, the value of P is equal to the mass fractal dimension D_m. The fibrillary morphology is consistent with the relatively low mass fractal dimension of the aggregates. For the agglomerates, the exponents are both greater than 3, indicating that agglomerates are surface fractals, *i. e.* dense particles with a fractal surface [33,34]. Given their gyration radius, the agglomerates would then be the constitutive elements of the large micrometric particles observed by low-magnification microscopy: their density is in accordance with the notion of surface fractals. The micrometric particles are indeed agglomerates of agglomerates: this is a fourth level of organization, which is too large to be observed by SAXS. The overall organization of the boehmite samples is summarized Fig. 4.

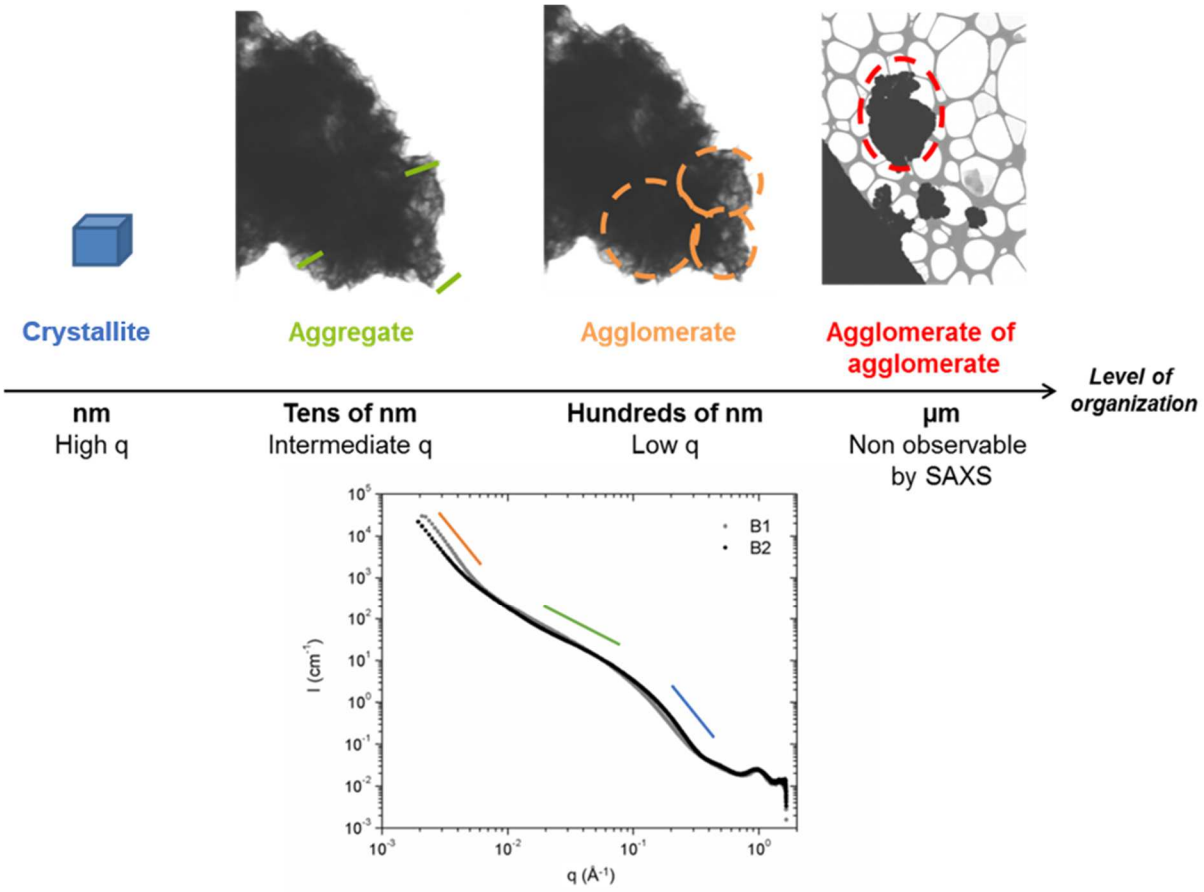

Fig. 4

The gyration radius of the crystallites for B1 and B2 are almost similar, their crystallite sizes being very close. The aggregates of the two gels are similar concerning the dimension and mass fractal dimension. The main difference is observed for the agglomerates: if they have the same gyration radius, the exponent is not the same. In the case of surface fractals, the surface fractal dimension D_s is provided by $D_s = 6 - P$ [32], which gives for B1 and B2 surface fractals dimensions of 2.3 and 2.6 respectively. The surface fractal dimension can be related to an average surface roughness of the agglomerates [33] and the surface of B2 agglomerates would then be rougher than for B1. The spatial arrangement of the fibrils is more aerated for B2, which can explain a greater surface roughness, and then a greater surface fractal dimension, for this sample. These observations are in accordance with the agglomeration and aggregation degrees. Both samples have the same aggregation degree, but different agglomeration degrees: agglomerates for B1 are more dense and composed with a higher number of aggregates.

3.2. Peptized samples

3.2.1. Visual observations

Fig. 5 shows the photographs of the different samples a few minutes after their preparation, and without any dilution.

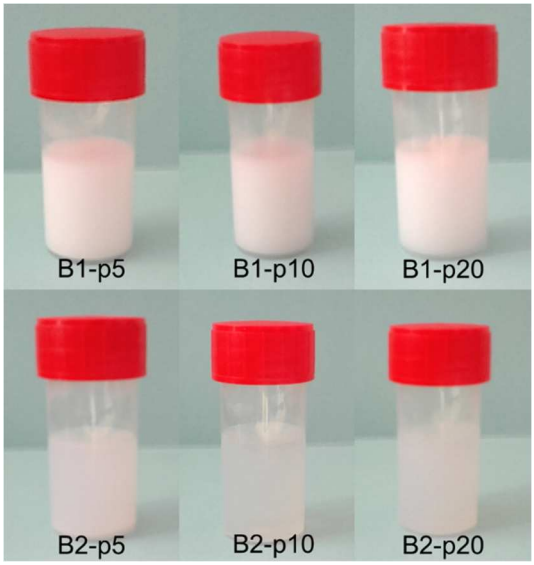

Fig. 5

A first visual observation of the samples reflects a different behavior as a function of the HNO_3/Al_2O_3 ratio and between the two boehmites. For boehmite B1, the three peptized samples are identically opaque, indicating the presence of at least micrometric particles which can diffuse visible light. For boehmite B2, the samples are more transparent than for B1, so made up of smaller particles, and the transparency is accentuated when the HNO_3/Al_2O_3 ratio increases, suggesting that a higher relative quantity of acid leads to a better dispersion of these large particles. For the sample B2-p20, a gelation is observed a few minutes after the preparation and for B1-p20, a few hours after.

3.2.2. Electron microscopy

Fig. 6 shows the STEM micrographs (SEM microscope) of the raw boehmite B1 and the corresponding peptized samples.

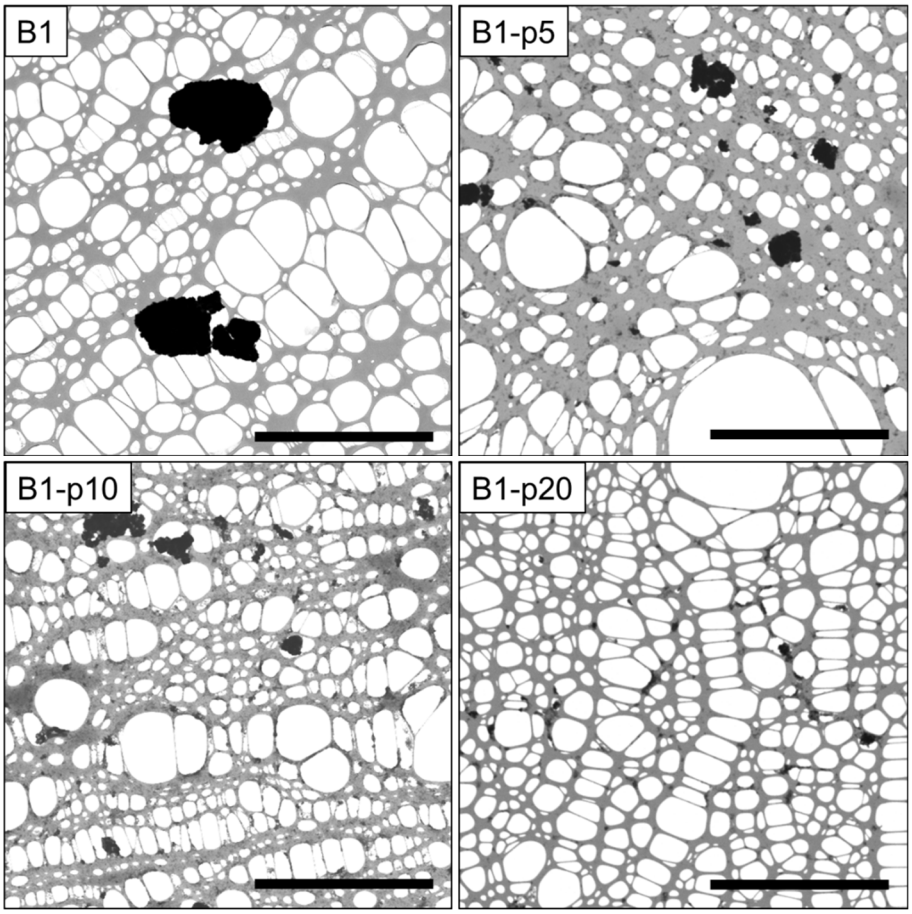

Fig. 6

When the HNO_3/Al_2O_3 ratio increases, due to the electrostatic repulsion, a progressive separation of the agglomerates of agglomerates is observed. For B1-p20, the particles which are still visible are around 1 µm large, in accordance with the remaining opacity of the sample (Fig. 5). Low-magnification micrographs for the samples B2 and B2-p5 are presented Fig. 7.

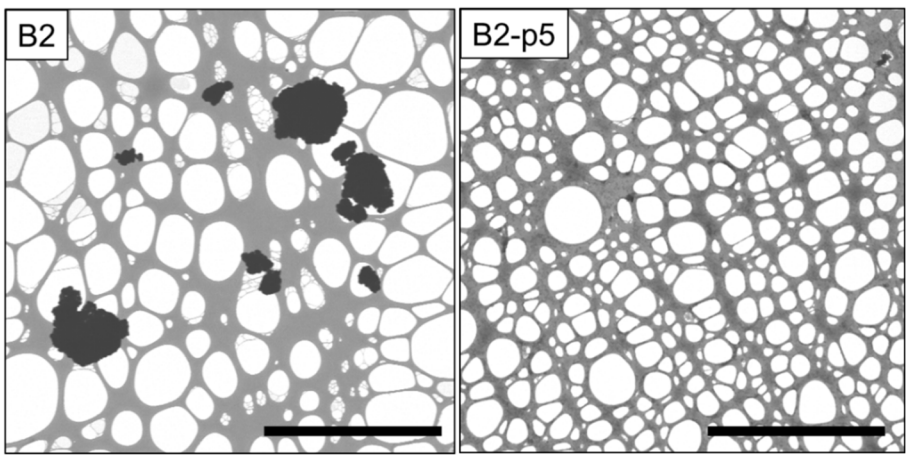

Fig. 7

The peptization, even for a low HNO_3/Al_2O_3 ratio of 5%, induces for B2, which is more peptizable, a drastic separation of the agglomerates of agglomerates: almost no particles are still visible for this magnification, which means that they are at least submicronic. Then, we did not find useful to show the micrographs for B2-p10 and B2-p20, which do not present any observable particle in these conditions of analysis.

Micrographs with higher magnifications of the raw boehmites and peptized samples are presented Fig. 8 for B1 and Fig. 9 for B2.

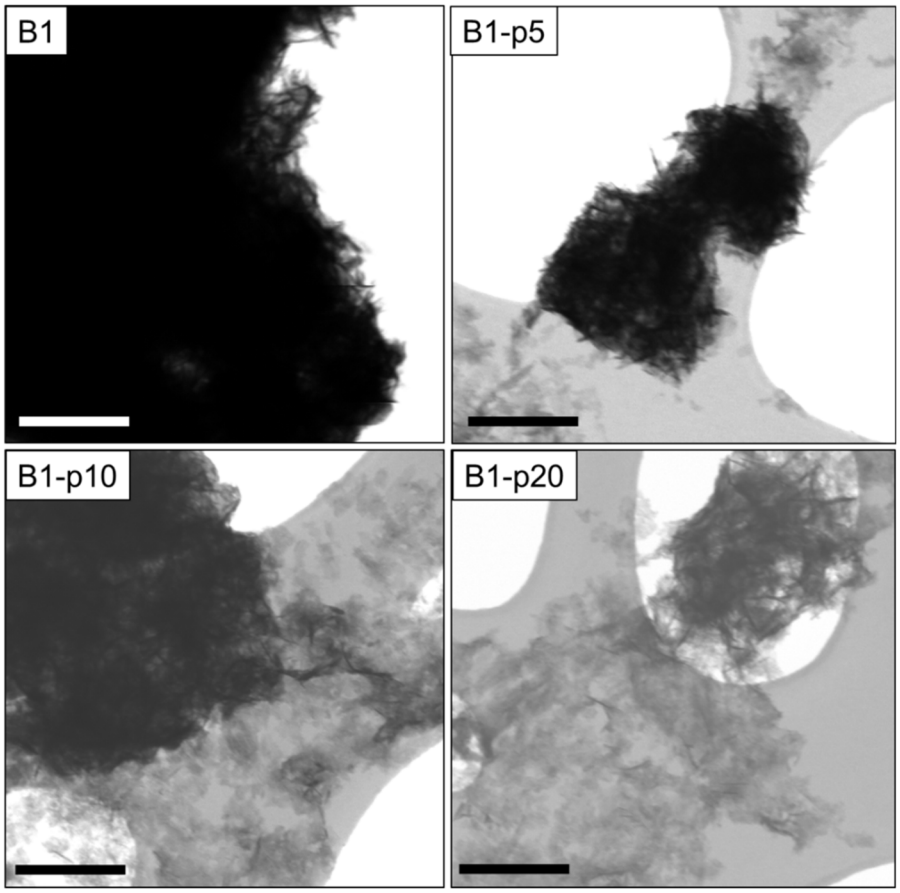

Fig. 8

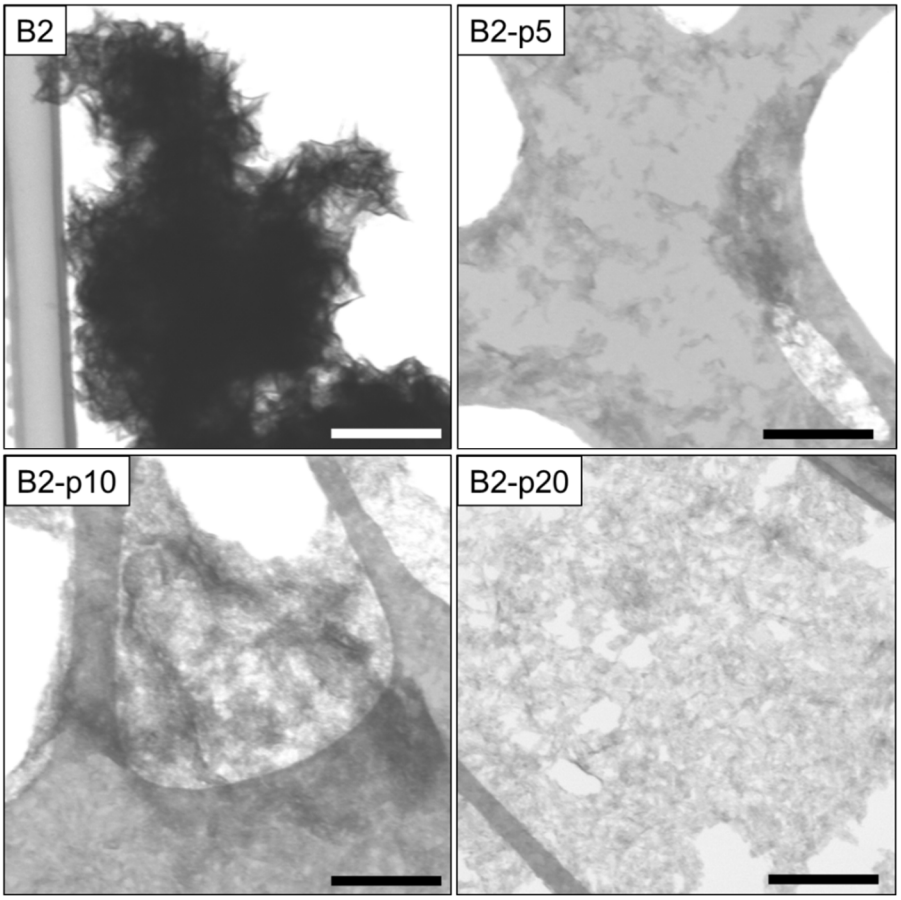

Fig. 9

Positive charging of boehmite surfaces lead to a separation between the aggregates. Isolated aggregates at the periphery of the agglomerates are observed, as same as an aeration of the structure of the agglomerates themselves. The effects of peptization are more accentuated when the HNO_3/Al_2O_3 ratio and the PI increase. For B2-p20, agglomerates seem to be completely dispersed and the sample is composed with a network of aggregates. These interconnected aggregates are consistent with the structure of a gel [19,20], and the rapid gelation observed for this sample.

The micrographs collected with the TEM microscope are shown Figs. 10 and 11.

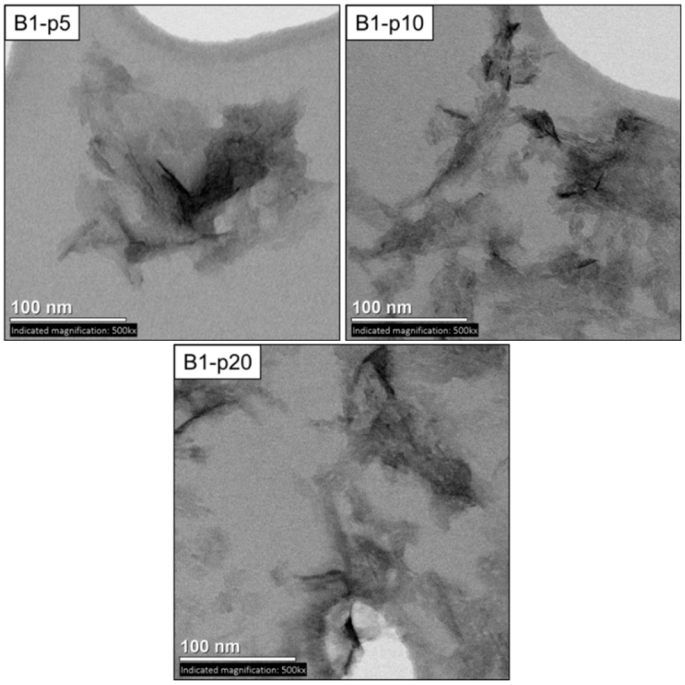

Fig. 10

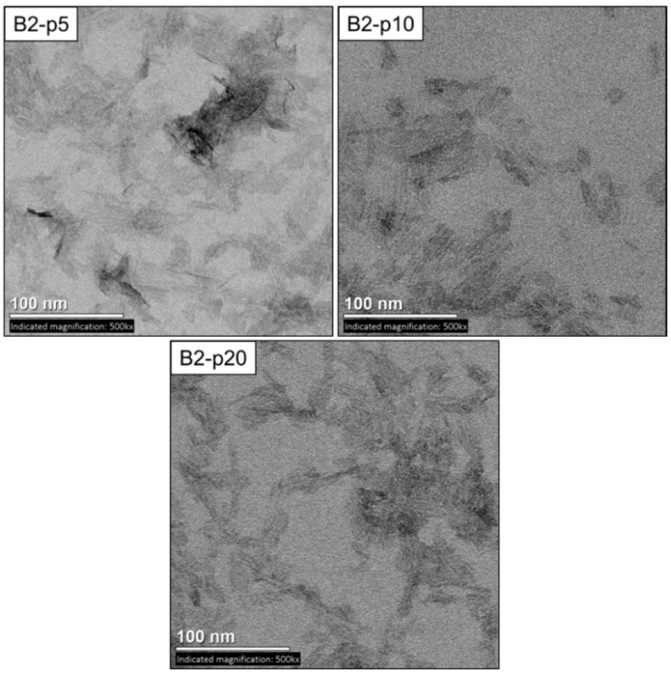

Fig. 11

The micrographs show the modification, for peptized samples, of aggregates through a progressive rearrangement of crystallites. Some small groups of crystallites (some tens of nanometers) seem to migrate under the effect of acid: they can either form quite disordered packings, or become more individualized. For the sample B2-p20, TEM shows a better observation of the interconnected chains forming the gel.

For the two samples, the combination of low- and high magnification micrographs in the SEM microscope and the micrographs from the TEM microscope lead to an observation of the effects of peptization on the different levels of organization of boehmites. The electrostatic repulsion caused by acidification separates the agglomerates, aggregates and crystallites, and the effects are enhanced with a higher acid quantity or a higher PI.

3.2.3. SAXS

SAXS curves for B1, B2 and the corresponding peptized samples are plotted on Figs. 12 and 13.

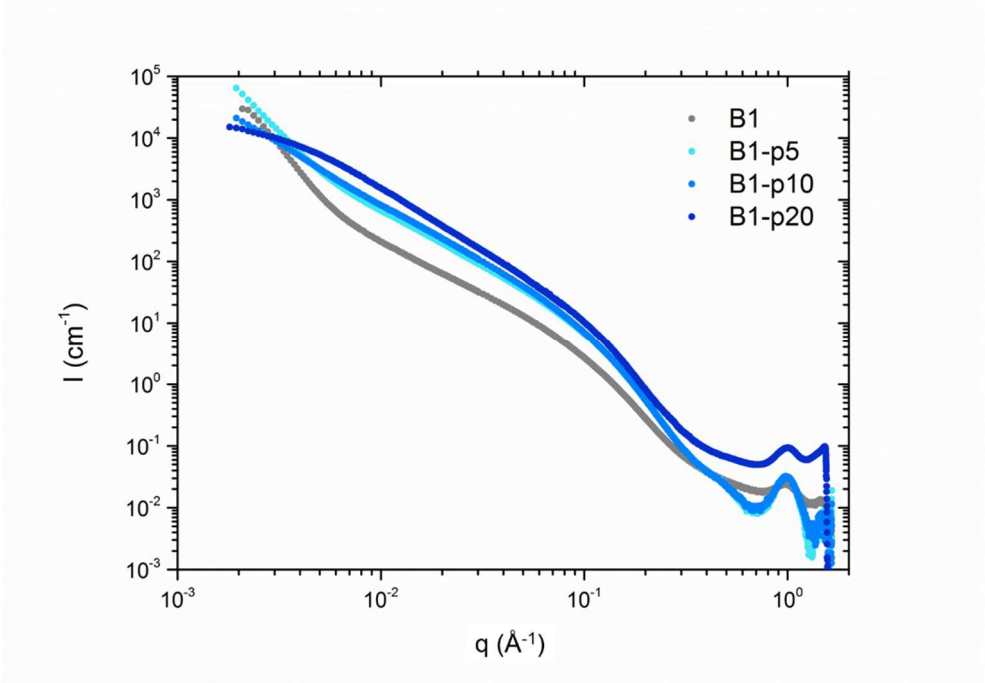

Fig. 12

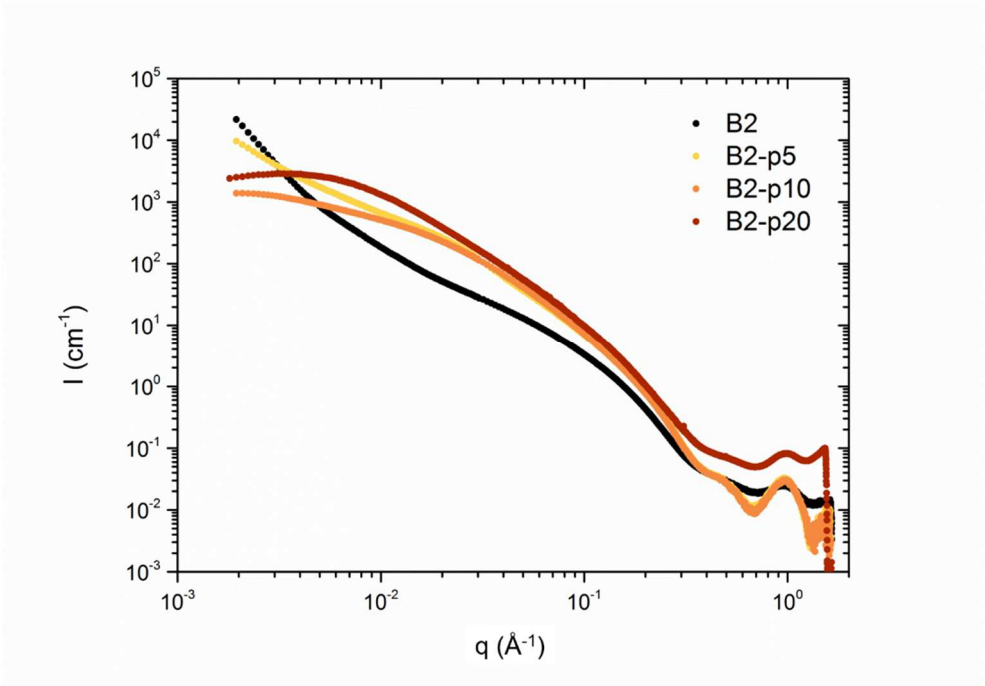

Fig. 13

The peptized samples, for B1 and B2, show the Porod domain and the aggregates domains as for the raw boehmites. However, important modifications are observed in the low q domain of the agglomerates. Especially for samples B2-p10 and B2-p20, the slope is very weak or even null: it is called Guinier plateau, and characterizes samples without agglomerates.
The gyration radii of the crystallites for the raw and peptized samples are in Table 2.

Table 2. Gyration radius of the crystallites for B1, B2 and corresponding peptized samples. Errors (±2σ) are indicated in brackets.

Sample	R_g crystallites (nm)	Sample	R_g crystallites (nm)
B1	1.22 *(0.08)*	B2	1.29 *(0.03)*
B1-p5	1.41 *(0.06)*	B2-p5	1.02 *(n.d.)*
B1-p10	1.34 *(0.11)*	B2-p10	1.02 *(0.6)*
B1-p20	1.50 *(0.05)*	B2-p20	1.22 *(n.d.)*

For each boehmite, the gyration radius of the crystallites does not vary significantly after peptization, and when the HNO_3/Al_2O_3 ratio varies. Then, the crystallite size is not modified by peptization, in accordance with the literature [10-12,16].

Data obtained from the Beaucage model for the domain of agglomerates of the samples are indicated in Table 3.

Table 3. Gyration radius R_g, exponent P of agglomerates and degree of agglomeration for B1, B2 and corresponding peptized samples. Errors (±2σ) are indicated in brackets.

Sample	R_g (nm)	P	z_{agglo}	Sample	R_g (nm)	P	z_{agglo}
B1	100 *(3)*	3.70 *(0.07)*	498	B2	107 *(3)*	3.39 *(0.03)*	325
B1-p5	125 *(4)*	3.20 *(0.05)*	478	B2-p5	93 *(n.d)*	2.28 *(n.d)*	41
B1-p10	152 *(5)*	2.44 *(0.05)*	270	B2-p10	107 *(14)*	2.17 *(0.06)*	9
B1-p20	143 *(8)*	1.53 *(0.07)*	9	B2-p20	-	-	-

For B1-5, the exponent P remains greater than 3: the sample keeps the density of a surface fractal, but its surface fractal dimension D_s = 2.8 indicates a higher surface roughness, probably caused by the higher spacing of the aggregates, in comparison with the raw boehmite. When the HNO_3/Al_2O_3 ratio reaches 10%, the value of P decreases below 3, which means that the agglomerates are considered as mass fractals. Because the separation of the aggregates is more effective, the agglomerates lose their density (and the degree of agglomeration decreases) and are detected as branched structures more than dense structures with a fractal surface, in accordance with electron microscopy observations. For B2, this transition is observed for a HNO_3/Al_2O_3 ratio of 5% only. For both boehmites, an increase of the HNO_3/Al_2O_3 ratio leads to an increase of the gyration radius of the agglomerates: they become larger due to a greater spacing between the aggregates, which is in accordance with the evolution of the agglomeration degree too. As expected from the shape of the corresponding curves, for the samples B1-p20 and B2-p20, agglomerates are almost not detected by SAXS. Either agglomerates are fully separated into aggregates and are then physically absent from the sample (it seems to be the case for B2-p20, which has a higher PI: microscopy does not show any agglomerates), or they become too large to be observed by SAXS in our conditions of analysis (for B1-p20, large agglomerates are still present but in

very small quantity as the degree of agglomeration is very low). A mechanism of evolution of the agglomerates is presented Fig. 14. For the sake of clarity, aggregates are represented as rods instead of branched structures.

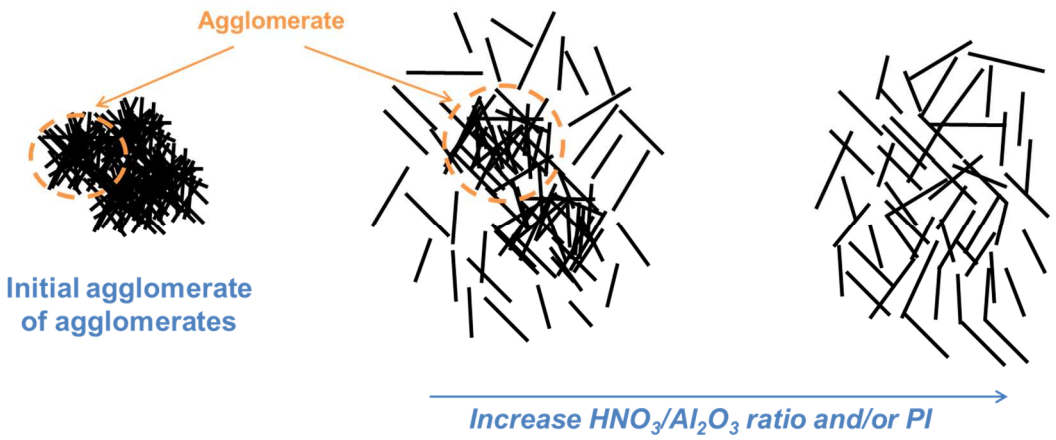

Fig. 14

The gyration radius and exponent P of the aggregates of raw boehmites and corresponding peptized samples are indicated Table 4.

Table 4. Gyration radius R_g and exponent P of aggregates and degree of aggregation for B1, B2 and corresponding peptized samples. Errors (±2σ) are indicated in brackets.

Sample	R_g (nm)	d_f	z_{ag}	Sample	R_g (nm)	d_f	z_{ag}
B1	12.3 *(0.3)*	1.94 *(0.01)*	88	B2	13.6 *(0.3)*	1.90 *(0.02)*	87
B1-p5	11.5 *(0.3)*	2.07 *(0.01)*	77	B2-p5	9.1 *(n.d.)*	2.28 *(n.d.)*	147
B1-p10	10.7 *(0.5)*	2.03 *(0.01)*	68	B2-p10	7.3 *(1)*	2.18 *(0.06)*	73
B1-p20	24.3 *(1.6)*	2.01 *(0.02)*	268	B2-p20	16. 9 *(n.d.)*	2.21 *(n.d)*	329

For HNO_3/Al_2O_3 = 5% or 10%, the average size of the aggregates decreases, especially for B2. The aggregates remain mass fractals. However, the fractal dimension first increases, which is also more accentuated for B2, and slightly decreases. Electron microscopy shows that peptization leads to a migration and rearrangement of small packs of crystallites. It is probable that these packs are preferentially separated from the outer branches of the aggregates: such a behavior has been reported for the aging of silica aggregates, where hydrolysis reactions take place and lead to a reorganization of the primary particles too [19,20]. One could imagine, due to the electrostatic repulsion, a migration of these small packs out of the aggregate, result in a less branched structure and a lower fractal dimension, as previously observed in the case of the separation of the agglomerates. Nevertheless, the aggregates are entangled to form agglomerates which remain dense even after peptization. Then, we believe that this entanglement prevents a free migration of the crystallites, and make them remain inside the aggregates and rearrange to form a more branched structure. This phenomenon would be predominant relative to the effective individualization of crystallites, and would explain the increase of the fractal dimension as same as the decrease of the size of the aggregates, which increases the aggregation degree. A partial dissolution of boehmite [17,18,23] could also contribute to create more disordered structures. The slight decrease of the fractal dimension for HNO_3/Al_2O_3 = 10% could be explain by an accentuated repulsion and a better freedom of migration inside the less dense agglomerates.

When HNO_3/Al_2O_3 = 20%, the dimension of the aggregates strongly increases for both boehmites. As previously exposed, in these conditions of peptization, agglomerates in B2 are completely dispersed and the sample is then an interconnected network of aggregates. Then, it explains why the dimension of the aggregate is much larger and the degree of aggregation much higher. The sample, in good accordance with the visual observations, is a transparent gel. For B1-p20, agglomerates are still present but in a very small quantity, as the degree of agglomeration is closed to 0. However, the concentration of the isolated aggregates seems to be sufficient to form a percolating network too, since the behavior of the aggregates is the same as for B2-p20. The sample is then composed of few agglomerates embedded in a gel structure: it remains opaque even after gelation. This gel structure is well characterized by SAXS as the B2-p20 SAXS curve has a typical gel-structure shape [25,35], with a first porod-domain at large q, a power-law domain that indicates the fractal dimension of the gel at medium q and a Guinier plateau at small q. Thus it can be deduce that the fractal dimension of the B2-p20 gel structure is 2.2, higher than the one of the B1-p20 equal to 2.0.

The effects of peptization on the aggregates are more accentuated for B2. The agglomerates being less dense, it favors their peptization, and we can suppose that the smaller crystallite size make them easier to separate from the aggregates.

A mechanism of peptization of the aggregates is presented Fig. 15. Gray crystallites are those which are separated from the initial aggregate.

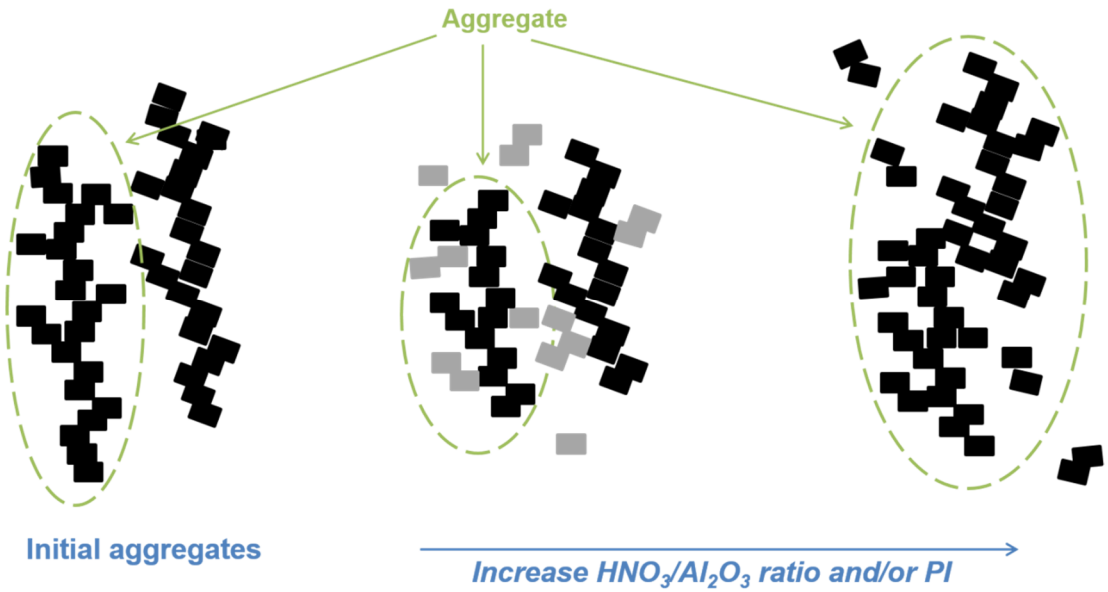

Fig. 15

The peptization affects the overall organization of boehmites: agglomerates of agglomerates, agglomerates and aggregates are modified. As expected, peptization is more effective with a higher quantity of acid, and with a higher PI.

3.3. Peptizable and non peptizable parts

The SAXS curves for peptizable (B1-p10-p) and non peptizable (B1-p10-np) parts are compared with B1-p10 on Fig. 16. Data providing from the fitting with the Beaucage model are listed on Table 5.

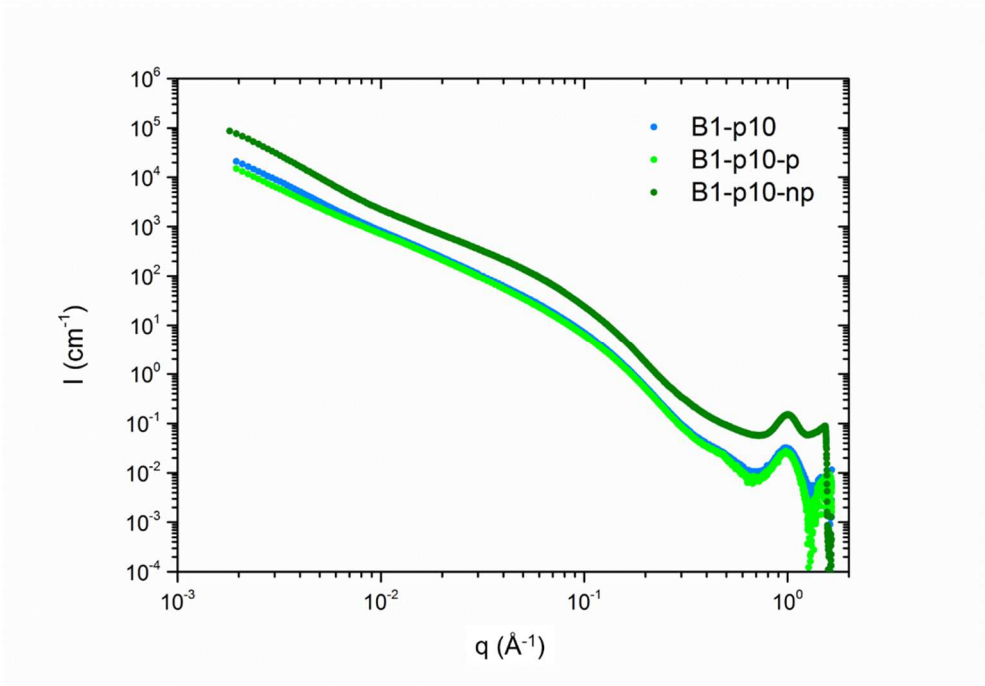

Fig. 16

Table 5. Gyration radius R_g and exponent P of agglomerates, aggregates and primary particles for samples B1-p10, B1-p10-p and B1-p10-np. Errors (±2σ) are indicated in brackets.

Sample	Agglomerates			Aggregates			Primary particles	
	R_g (nm)	P	z_{agglo}	R_g (nm)	P	z_{ag}	R_g (nm)	P
B1-p10	152 *(5)*	2.44 *(0.05)*	270	10.7 *(0.5)*	2.03 *(0.01)*	68	1.34 *(0.11)*	4.0
B1-p10-p	100	2.36 *(0.03)*	63	10.7 *(0.4)*	2.06 *(0.02)*	80	1.28 *(0.12)*	4.0
B1-p10-np	110	2.38 *(0.05)*	343	6.0 *(1.4)*	1.95 *(0.14)*	16	1.46 *(0.36)*	4.0

It is worth noting that no difference is observed for the fractal dimension for the agglomerates and aggregates of the peptized sample and its peptizable and non peptizable part. The main distinctions are located on the dimensions of the structures. We can notice that the dimensions for the agglomerates of the centrifuged samples are smaller than for B1-p10: during centrifugation, the heavier then bigger agglomerates (so the agglomerates with a very high agglomeration degree) tend to stick to the walls of the tube, especially for the sediment, which

can explain this trend. Agglomerates for B1-p10-np are composed with smaller aggregates (and their agglomeration degree is high), so form the dense sediment instead of remaining in suspension. For B1-p10-p, agglomerates are smaller with a low agglomeration degree and formed with bigger aggregates, so light enough to remain in the supernatant. One can finally note that the presence of agglomerates is consistent with a PI different from 100%, contrary to the sample B2-p10 which is only composed with aggregates.

The PI measurement separates particles as a function of their difference of density, which explains the differences observed by SAXS between B1-p10-p and B1-p10-np. For B1, agglomerates of agglomerates are larger so more difficult to separate by chemical and mechanical action, and are still present after peptization, as shown by microscopy. The agglomerates themselves are more dense than for B2, which is 100% dispersible and the action of acid is disadvantaged. Then, peptization with identical conditions leaves larger and denser particles for B1 than for B2, which will lead to a less concentrated supernatant and the measure of a lower PI. Then, PI seems to be mainly governed by the density of the agglomerates of boehmite.

4. Conclusion

This work is focused on the mechanisms of peptization of boehmite, an essential step during the fabrication of alumina catalyst supports. Two boehmites with different peptization index are peptized with different acid/aluminum ratios. The resulting samples are studied by coupling STEM and SAXS analysis, which provides a multi-scale characterization of the overall structure of the samples.

During peptization, the creation of an electrostatic repulsion between the positively charged surface hydroxyl groups of boehmite lead to modifications of the boehmite morphology. The micrometric agglomerates of agglomerates are separated to form individualized agglomerates, which become themselves more aerated by dispersion of the aggregates: this effect can lead to a full dispersion of agglomerates in interconnected aggregates, and to the gelation of the samples. Lastly, aggregates tend to become more disordered due to a migration and rearrangement of crystallites probably caused by steric hindrance and partial dissolution. An interesting point is the difference of the effects of peptization inside the agglomerates and aggregates, even if the phenomenon of repulsion remains the same. Then, two separated

mechanisms of peptization, depicting the behavior of the agglomerates and aggregates, when in contact with acid medium, are proposed.

As expected, the effects of peptization are more accentuated when the acid/aluminum ratio increases, and on the boehmite which presents the higher peptization index: these results denote the importance of the initial properties of the boehmite in the elaboration process of the supports. We can notice that even for a little difference (about 20%) in the value of PI, marked differences are observed in the evolution of the two boehmites.

In order to go further concerning the determination of PI, the peptizable and non peptizable parts obtained after centrifugation of one of the samples were studied by SAXS. The separation by difference of density of the particles is confirmed, and the difference of structure between the two boehmites explains the variation of the PI. The key point, for the PI of boehmite, seems to be the density of the agglomerates.

The multi-scale vision of peptization provided by coupling STEM and SAXS analysis constitutes a starting point for an accurate analysis of boehmite during the whole fabrication process of the alumina catalysts supports. It can be extended to the study of solid-state peptization really occurring during the kneading-extrusion process, and the study of the neutralization step. This better understanding of the modifications of the boehmite organization in the presence of an acid and, by extension, a base, could be of importance for the optimization of the structure of the final catalyst support.

Acknowledgements

This work was supported by IFPEN.

References

[1] P. Euzen, P. Raybaud, X. Krokidis, H. Toulhoat, J.- P. Jolivet, C. Froidefond, Handbook of porous solids, Wiley (2002) 1591-1677.
https://doi.org/10.1002/9783527618286.ch23b

[2] M. F. L. Johnson, J. Mooi, The origin and type of pores in some alumina catalysts, J. Catal. 10 (4) (1968) 342-354.
https://doi.org/10.1016/0021-9517(68)90149-8

[3] S. J. Wilson, The dehydration of boehmite γ-AlOOH to γ-Al_2O_3, J. Solid State Chem. 30 (2) (1979) 247-255.

https://doi.org/10.1016/0022-4596(79)90106-3
[4] R. Poisson, J. P. Brunelle, P. Nortier, Catalyst supports and supported catalysts: theoretical and applied concepts, Ed. Stiles Boston (1987) 11-55.
https://doi.org/10.1002/aic.690340129
[5] E. Weiland, M. A. Springel-Huet, A. Nossov, F. Guenneau, A. A. Quoineaud, A. Gédéon, Exploring the complex porosity of transition aluminas by ^{129}Xe NMR spectroscopy, J. Phys. Chem. C 119 (27) (2015) 15385-15291.
https://doi.org/10.1021/acs.jpcc.5b03211
[6] E. M. Forman, M. A. Trujillo, K. J. Ziegler, S. A. Bradley, H. Wang, S. Prabhakar, S. Vasenkov, Self-diffusion of heptane inside aggregates of porous alumina particles by pulsed field gradient NMR, Micropor. Mesopor. Mat. 229 (2016) 117-123.
https://doi.org/10.1016/j.micromeso.2016.04.027
[7] S. Kolitcheff, E. Jolimaître, A. Hugon, J. Verstraete, P. L. Carrette, M. Tayakout-Fayolle, Tortuosity of mesoporous alumina catalysts supports: influence of the pore network organization, Micropor. Mesopor. Mat. 248 (2017) 91-98.
https://doi.org/10.1016/j.micromeso.2017.04.010
[8] P. Raybaud, M. Digne, R. Iftimie, W. Wellens, P. Euzen, H. Toulhoat, Morphology and surface properties of boehmite (γ-AlOOH): a density functional theory study, J. Catal. 201 (1) (2001) 236-246.
https://doi.org/10.1006/jcat.2001.3246
[9] E. Morgado, Y. L. Lam, S. M. Menezes, L. F. Nazar, Characterization of peptized boehmite systems: a ^{27}Al nuclear magnetic resonance study, J. Colloid Interf. Sci. 176 (2) (1995) 432-441.
https://doi.org/10.1006/jcis.1995.9948
[10] P. Alphonse, M. Courty, Surface and porosity of nanocrystalline boehmite xerogels, J. Colloid Interf. Sci. 290 (1) (2005) 208-219.
https://doi.org/10.1016/j.jcis.2005.04.013
[11] Y. Zheng, J. Song, X. Xu, M. He, Q. Wang, L. Yan, Peptization mechanism of boehmite and its effect on the preparation of a fluid cracking catalyst, Ind. Eng. Chem. Res. 53 (24) (2014) 10029-10034.
https://doi.org/10.1021/ie501060g
[12] F. Karouia, M. Boualleg, M. Digne, P. Alphonse, Control of the textural properties of nanocrystalline boehmite regarding its peptization ability, Powder Technol. 237 (2013) 602-609.

https://doi.org/10.1016/j.powtec.2012.12.054
[13] D. Fauchadour, F. Kolenda, L. Rouleau, L. Barré, L. Normand, Peptization mechanisms of boehmite used as precursor for catalysts, Stud. Surf. Sci. Catal. 143 (2002) 453-461.
DOI: 10.1016/S0167-2991(00)80686-2
[14] J. Nair, P. Nair, J. G. van Ommen, J. R. Ross, A. J. Burggraaf, F. Mizukami, Influence of peptization and ethanol washing on the pore structure evolution of sol-gel-derived alumina catalysts supports, J. Am. Ceram. Soc. 81 (10) (1998) 2709-2712.
https://doi.org/10.1111/j.1151-2916.1998.tb02681.x
[15] J. M. Drouin, T. Chopin, P. Nortier, H. Van Damme, Rheology and structure of peptizable boehmite pastes, J. Colloid Interf. Sci. 125 (1) (1988) 314-326.
[16] P. Alphonse, M. Courty, Structure and thermal behavior of nanocrystalline boehmite, Thermochim. Acta 425 (1-2) (2005) 75-89.
https://doi.org/10.1016/j.tca.2004.06.009
[17] T. Assih, A. Ayral, M. Abenoza, J. Phalippou, Raman study of alumina gels, Journal of Materials Science 23 (9) (1988) 3326-3331.
https://doi.org/10.1007/BF00551313
[18] R. I. Zakharchenya, Influence of peptization on the properties of alumina produced from boehmite sols, J. Sol-gel Sci. Techn. 6 (2) (1996) 179-186.
https://doi.org/10.1007/BF00425975
[19] P. W. G. J. Wijnen, T. P. M. Beelen, K. P. J. Rummens, H. C. P. L. Saeijs, J. W. de Haan, L. Van den Wen, R. A. Van Santen, The molecular basis of aging of aqueous silica gel, J. Colloid Interf. Sci. 145 (1991) 17-32.
https://doi.org/10.1016/0021-9797(91)90097-R
[20] R. A. Van Santen, T. P. M. Beelen, H. F. Van Garderen, W. H. Dokter, E. Pantos, Aggregation and aging in silica gel, Nucl. Instrum. Meth. B 97 (1995) 231-237.
https://doi.org/10.1016/0168-583X(95)00194-8
[21] P. Riello, A. Minesso, A. Craievich, A. Benedetti, Synchrotron SAXS study of the mechanisms of aggregation of sulfate zirconia sols, J. Phys. Chem. B 107 (15) (2003) 3390-3399.
https://doi.org/10.1021/jp027432b
[22] F. Rashidi, A. N. Kharat, A. M. Rashidi, E. Lima, V. Lara, J. S. Valente, Fractal geometry approach to describe mesostructured boehmite and gamma-alumina nanorods, Eur. J. Inorg. Chem. 2010 (10) (2010) 1544-1551.
https://doi.org/10.1002/ejic.200901103

[23] D. W. Schaefer, T. Rieker, M. Agamalian, J. S. Lin, D. Fischer, S. Sukumaran, C. Chen, G. Beaucage, C. Herd, J. Ivie, Multilevel structure of reinforcing silica and carbon, J. Appl. Crystallogr. 33 (2000) 587-591.
https://doi.org/10.1107/S0021889800001199
[24] G. Beaucage, D. W. Schaefer, Structural studies of complex systems using small-angle scattering: a unified Guinier/power-law approach, J. Non-Cryst. Solids 172-174 (1994) 797-805.
https://doi.org/10.1016/0022-3093(94)90581-9
[25] G. Beaucage, Small-angle scattering from polymeric mass fractals of arbitrary mass fractal dimension, J. Appl. Crystallogr. 29 (2) (1996) 134-146.
https://doi.org/10.1107/S0021889895011605
[26] H. K. Kammler, G. Beaucage, R. Mueller, S. E. Pratsinis, Structure of flame-made silica nanoparticles by ultra-small-angle X-ray scattering, Langmuir 20 (5) (2004) 1915-1921.
https://doi.org/10.1021/la030155v
[27] J. E. Dennis, D. M. Gay, R. E. Welsch, An adaptative non linear least-squares algorithm, ACM Trans. Math. Softw. 7 (1981) 348-368.
[28] A. Guinier, G. Fournet, Small angle scattering of X-rays, Wiley, New York, 1955.
https://doi.org/10.1002/pol.1956.120199326
[29] H. K. Kammler, G. Beaucage, D. J. Kohls, N. Agashe, J. Ilavsky, Monitoring simultaneously the growth of nanoparticles and aggregates by in-situ small-angle X-ray scattering, J. Appl. Phys. 97 (2005) 054309.
https://doi.org/10.1063/1.1855391
[30] D. W. Schaefer, J. E. Martin, P. Wiltzius, D. S. Cannell, Fractal geometry of colloidal aggregates, Phys. Rev. Lett. 52 (26) (1984) 2371-2374.
https://doi.org/10.1103/PhysRevLett.52.2371
[31] P. Meakin, Formation of fractal clusters and networks by irreversible diffusion-limited aggregation, Phys. Rev. Lett. 51 (13) (1983) 1119-1123.
https://doi.org/10.1103/PhysRevLett.51.1119
[32] D. A. Weitz, J. S. Huang, M. Y. Lin, J. Sung, Limits of the fractal dimension for irreversible kinetic aggregation of gold colloids, Phys. Rev. Lett. 54 (13) (1985) 1416-1419.
https://doi.org/10.1103/PhysRevLett.54.1416
[33] H. D. Bale, P. W. Schmidt, Small-angle X-ray scattering investigation of submicroscopic porosity with fractal properties, Phys. Rev. Lett. 53 (6) (1984) 596-599.
https://doi.org/10.1103/PhysRevLett.53.596

[34] P. Pfeifer, Fractal dimension as working tool for surface roughness problems, Applications of Surface Science 18 (1-2) (1984)146-164.
https://doi.org/10.1016/0378-5963(84)90042-4
[35] T. P. M. Beelen, P. Wijnen, C. G. Vonk, R. A. Van Santen, SAXS study of silica gel formation from aqueous silicate solutions, Catal. Lett. 3 (1989) 209-215.
https://doi.org/10.1007/BF00766395

Figure captions

Fig. 1. SAXS curves for samples B1 and B2.

Fig. 2. Example of SAXS curve fitting using the Beaucage model on samples a) B1 and b) B2: experimental and simulated curve, and individual contributions of agglomerates, aggregates and primary particles.

Fig. 3. STEM bright-field micrographs (SEM microscope) of the raw samples B1 and B2.

Fig. 4. Structural organization of the boehmite samples.

Fig. 5. Photographs of the peptized samples.

Fig. 6. STEM bright-field micrographs (SEM microscope) of samples B1, B1-p5, B1-p10 and B1-p20. Scale bar: 10 µm.

Fig. 7. STEM bright-field micrographs (SEM microscope) of samples B2 and B2-p5. Scale bar: 10 µm.

Fig. 8. STEM bright-field micrographs (SEM microscope) of the samples B1, B1-p5, B1-p10 and B1-p20. Scale bar: 250 nm.

Fig. 9. STEM bright-field micrographs (SEM microscope) of the samples B2, B2-p5, B2-p10 and B2-p20. Scale bar: 250 nm.

Fig. 10. STEM bright-field micrographs (TEM microscope) of samples B1-p5, B1-p10 and B1-p20.

Fig. 11. STEM bright-field micrographs (TEM microscope) of samples B2-p5, B2-p10 and B2-p20.

Fig. 12. SAXS curves of samples B1, B1-p5, B1-p10 and B1-p20.

Fig. 13. SAXS curves of samples B2, B2-p5, B2-p10 and B2-p20.

Fig. 14. Evolution of the agglomerates during peptization.

Fig. 15. Evolution of the aggregates during peptization.

Fig. 16. SAXS curves of the samples B1-p10-p and B1-p10-np.

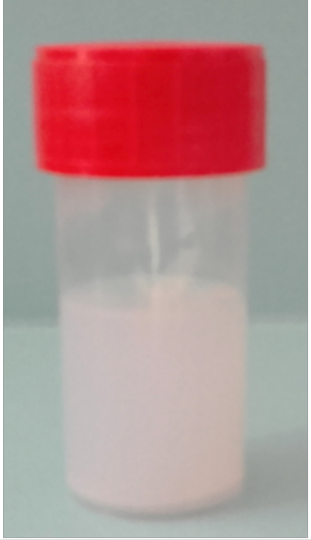

HNO_3